Direct Growth of High Mobility and Low Noise Lateral MoS₂-Graphene Heterostructure Electronics

Amirhossein Behranginia[1], Poya Yasaei[1], Arnab K. Majee[2], Vinod K. Sangwan[3], Fei Long[4], Cameron J. Foss[2], Tara Foroozan[5], Shadi Fuladi[6], Mohammadreza Hantehzadeh[1], Reza Shahbazian-Yassar[1], Mark C. Hersam[3,7], Zlatan Aksamija[2]*, Amin Salehi-Khojin[1]*

[1]Department of Mechanical and Industrial Engineering, University of Illinois at Chicago, Chicago, IL, 60607, USA

[2]Electrical and Computer Engineering Department, University of Massachusetts Amherst, Amherst, Massachusetts 01003, United States

[3]Department of Materials Science and Engineering, Northwestern University, Evanston, Illinois 60208, USA

[4]Department of Mechanical Engineering, University of Michigan Tech, Houghton, MI, 49931, USA

[5]Department of Civil and Material Engineering, University of Illinois at Chicago, Chicago, IL, 60607, USA

[6]Department of Physics, University of Illinois at Chicago, Chicago, IL, 60607, USA

[7]Department of Chemistry, Northwestern University, Evanston, Illinois 60208, USA

 [*] Corresponding author, salehikh@uic.edu, zlatana@engin.umass.edu

ABSTRACT

Reliable fabrication of lateral interfaces between conducting and semiconducting 2D materials is considered a major technological advancement for the next generation of highly-packed all-2D electronic circuitry. In this report, we employed seed-free consecutive chemical vapor deposition (CVD) processes to synthesize high-quality lateral MoS₂-graphene heterostructures and comprehensively investigated their electronic properties through a combination of various experimental techniques and theoretical modeling. Our results show

that the MoS$_2$-graphene devices exhibit an order of magnitude higher mobility and lower noise metrics compared to conventional MoS$_2$-metal devices as a result of energy band rearrangement and smaller Schottky barrier height at the contacts. These findings suggest that MoS$_2$-graphene in-plane heterostructures are promising materials for the scale-up of all-2D circuitry with superlative electrical performance.

1. INTRODUCTION

According to Moore's law, the transistor count per chip doubles every two years.[1] The continuing shrinkage in size is pushing the silicon-based industry toward its physical limitations. Numerous efforts are now being dedicated to the development of two-dimensional (2D) materials for future electronic/optoelectronic devices.[2–8] Transition metal dichalcogenides (TMDs) are a family of layered crystals that are opening the possibility of developing systems with reduced dimensionality and a range of unique properties.[8] The most abundant member of this family is molybdenum disulfide (MoS$_2$), which shows interesting semiconducting properties[9,10] that make it a promising candidate for digital electronic circuitry applications. On the downside, the electrical performance of MoS$_2$ field-effect transistors (FETs) has been limited by the performance of the MoS$_2$ junction with the metal contact electrodes.[11] In particular, due to Fermi level pinning, nearly all metals form a Schottky barrier upon contact with MoS$_2$, which results in large contact resistances on the extrinsic (2-probe) performance of MoS$_2$-based devices.[11] Additionally, metals do not possess sufficient mechanical bendability for use in flexible structures. Thus, significant research has been invested in finding a replacement for conventional metal electrodes that will allow the fabrication of intrinsically 2D devices with improved device metrics.[12–17]

In this study, we utilize seed-free consecutive CVD processes to synthesize lateral MoS$_2$-graphene interfaces with large crystal domain sizes and high interface quality. Device-level

experiments reveal that the extrinsic mobility of MoS_2-graphene FETs is improved by an order of magnitude compared with the MoS_2-metal FETs because of energy band rearrangement and smaller Schottky barrier height at the contacts, especially in the accumulation region (large positive gate voltages). For direct verification of the device-level measurements and to gain more insight into the role of the interface on the overall resistance of the device, Kelvin probe force microscopy (KPFM) is employed to map the surface potential distribution of a biased MoS_2-graphene heterojunction under applied gate potentials. Low frequency 1/f noise metrics of the MoS_2-graphene FETs are also extensively studied in both subthreshold and accumulation regions to identify the origins of signal fluctuations in lateral MoS_2-graphene devices. The results show that the mobility fluctuations are the dominant origin of the noise in the accumulation region, while the overall noise amplitude is an order of magnitude lower than MoS_2-metal FETs. Additionally, electrostatic breakdown measurements are performed on both MoS_2-graphene and MoS_2-metal devices to study the failure modes of the devices under high-power operation. To gain insight into the physics of the observed improvements, the interfacial resistance is modeled using a combination of first-principles band structure calculations, followed by calculation of the transmission coefficient and interfacial conductance in the Landauer formalism. Overall, this work establishes the superlative electronic properties of directly grown MoS_2-graphene lateral heterostructures.

2. RESULTS AND DISCUSSION

In our method, a graphene film with partial (or full) coverage is initially synthesized on a copper substrate in an atmospheric pressure chemical vapor deposition (AP-CVD) process and then transferred to a silicon (SiO_2/Si) substrate, similar to our previous reports.[18,19] The samples are then transferred to another AP-CVD chamber to synthesize MoS_2 through the reaction of sulfur and molybdenum trioxide (MoO_3) precursors. **Figure 1a-b** shows the

CVD-grown MoS_2 triangular single crystalline flakes making a lateral junction with graphene domains. The polycrystalline MoS_2 film is also grown next to the graphene flakes by increasing the MoS_2 growth time (Figure S1). We note that even without any specific surface treatment (e.g., use of seed promoters), the growth of MoS_2 is more favorable on a bare oxide substrate compared to graphene films. This observation may be explained by the relative scarcity of nucleation sites on graphene compared to SiO_2. The preferential deposition on SiO_2 causes the growth of MoS_2 to stop right at the edge of the graphene film, resulting in a lateral (in-plane) heterojunction. We note that due to the lattice mismatch between graphene and MoS_2, an atomically sharp interface is not likely to form, but due to the self-limiting growth process (deposition selectivity), the overlapped region remains quite small (2 to 30 nm).[20] Atomic force microscopy (AFM) characterization (Figure S2) also shows an overlapped region between MoS_2 and graphene domains which is smaller than 30 nm over the entire interface length. We also found that a uniform MoS_2 film can fill arbitrary-shaped patterns in the graphene films and form lateral interfaces (Figure 1c). Raman point spectroscopy on a patterned MoS_2-graphene interface shows the characteristic peaks of MoS_2 and graphene next to the silicon peaks from the substrate (Figure 1d). The inset of Figure 1d (right) shows the spatial distributions of the graphene and MoS_2 Raman peaks, which reveal the formation of a lateral interface without a noticeable gap or overlap. The classical least-square (CLS) fitting was used to analyze the obtained hyper-spectra, including the E^2_g and A^1_g peaks of the MoS_2 (coded as green in Figure 1d) and the G peak of the graphene (coded as red).

Next, we fabricated back-gated field-effect transistors (FETs) by patterning metal electrodes on the graphene films rather than on the MoS_2 channel (Figure 1e-f). Figure S3 shows the two-probe current-voltage (I_d-V_{ds}) measurements at a back gate bias (V_g) of 60 V for

different temperatures. To compare the linearity of the I_d-V_{ds} trends in the MoS_2-graphene and MoS_2-metal FETs, the normalized I_d-V_{ds} trends (Y axis: $I_d/I_{d@Vsd=1V}$) at temperature 270 K are shown as an inset to Figure 1g. Unlike the MoS_2-metal device, the MoS_2-graphene FET shows a linear behavior. The correlation coefficient of the linear regression (R_{square}) in the I_d-V_{ds} is also calculated for both devices at different temperatures (see Figure 1g). The R_{square} of the MoS_2-graphene FET starts from 1 at room temperature and goes to 0.970 at 40 K. However, the R_{square} of the MoS_2-metal transistor shows greater temperature dependence (0.998 to 0.799). The larger non-linearity in the I_d-V_{ds} curve of the MoS_2-metal device compared to the MoS_2-graphene device – especially at low temperatures – suggests that a larger Schottky barrier is present for the metal-contacted MoS_2 device.

The output characteristics for both devices at different gate biases for different temperatures are also shown in Figure S4. Moreover, the electrical transfer characteristics (I_d-V_g) were measured at different temperatures (Figure S5) and a typical n-type semiconducting behavior was obtained for both devices. The I_d-V_g results at 270 K (Figure 1h) indicate that the current density ($I_d \times \frac{L}{W}$) at $V_g = 80$ V for the MoS_2-graphene FET is 20 times higher than the MoS_2-metal FET. This ratio becomes even larger at low temperatures and approaches ~74 times at 40 K (Figure 1h inset), which is attributed to a smaller barrier for thermally induced charge carriers in the MoS_2-graphene in-plane heterostructure. The extrinsic field-effect mobility is also calculated for both structures at room temperature and different back gate voltages (Figure S6a). Both transistors are completely turned OFF at large negative gate biases and turned ON at a threshold voltage of 55 V and 40 V with an ON/OFF ratio of 10^4 and 10^5 for MoS_2-metal and MoS_2-graphene, respectively. The linear field-effect mobility is calculated as ~11.5 cm^2/V.S for MoS_2-graphene and ~1.5 cm^2/V.S for MoS_2-metal at $V_g = 80$ V. It should be noted that the field-effect mobility of the MoS_2-metal devices is consistent with the

previously reported mobility of monolayer CVD MoS_2 without top-gate dielectrics.[13] However, higher extrinsic mobility values can be achieved by using multilayer MoS_2[21] or using high-k dielectric substrates/overcoats.[22] Our temperature-dependent measurements show that the mobility of the MoS_2-metal FET is reduced by 95% as the temperature is decreased to 40 K, while the MoS_2-graphene FET shows almost constant mobility down to 160 K and then 30% reduction in the mobility at 40 K (Figure S6b). This temperature dependence is also demonstrated in the inset of Figure 1h in which the drain current of the MoS_2-graphene device reduces by ~4 times, while that of the MoS_2-metal device decreases by ~26 times.

To gain better insight concerning the Schottky barrier height, a 2D thermionic model is used to analyze the data.[23] Figure S7 shows the logarithmic plots of $(I_d/T^{3/2})$ versus $(1000/T)$ for the MoS_2-graphene and MoS_2-metal interfaces at different V_{ds} and different back gate biases (SI file, section 7-9). In Figure S9, a switch in the sign of the slope at V_g = ~60 V reveals the absence of the Schottky barrier for the MoS_2-graphene in-plane contact at large gate voltages. Figure 1i further shows the derived Schottky barrier height of both structures at room temperature for different applied gate voltages. The Schottky barrier height for the MoS_2-metal structure is about 88 meV at V_g = 10 V and decreases to 60 meV for V_g = 60 V, while the MoS_2-graphene in-plane heterostructure starts at ~58 meV at V_g = 10 V and fades to zero at V_g = 60 V.

We also performed Kelvin probe force microscopy (KPFM) experiments to map the surface potential distribution across the MoS_2-graphene interface under applied source-drain and gate voltages (setup is shown in SI file, Figure S10). This technique enables us to spatially map the local potential drops in the MoS_2-graphene lateral heterojunction and in the MoS_2 and graphene films under device operational conditions to gain insight into their relative

contributions to the overall resistance of the device. Figure 2a shows the KPFM mapping of the device at $V_{ds} = 0$ V and $V_g = 0$ V. We also mapped the change in the surface potential along the entire length of the device at $V_{ds} = 1$V and at different gate voltages (Figure 1b-c). As the gate voltage increases from -20 V to +20 V, the potential drop across the interface decreases from 455 mV to 201 mV (Figure 1d). This observation implies that the contribution of the resistive potential drop across the interface relative to the total resistance of the device decreases as one increases the gate voltage. In other words, the MoS_2-graphene contact resistance has a negligible contribution to the overall device resistance at larger gate voltages.

Next, a systematic study of 1/f noise was performed in the MoS_2-graphene and MoS_2-metal devices in a vacuum (pressure $< 10^{-5}$ Torr). Low frequency 1/f noise has the potential to severely limit the performance of nanoscale materials because 1/f noise increases with decreasing number of carriers (i.e., device size). Recently, it has been shown that metal contacts can play a significant role in 1/f noise in CVD-grown MoS_2. Thus, 1/f noise is an important metric to gauge the quality and viability of lateral graphene-MoS_2 heterojunctions. Regardless of the fundamental sources of 1/f noise (i.e., mobility fluctuation versus carrier number fluctuation), the noise power spectral density S_I can be described empirically as:

$$S_I = \frac{AI^\gamma}{f^\beta}$$

where I is mean drain current, f is frequency, A is noise amplitude, and exponents β and γ are expected to be close to ideal values of 1 and 2, respectively. Figure 3a shows $1/f^\beta$ dependence of noise spectral density for a MoS_2-graphene device with $\beta = 1.02 \pm 0.002$ over four decades of frequency. For more thorough analysis, the noise measurement was limited to $1 - 100$ Hz and β was found to be in the range 1.0 ± 0.2 for all measured devices. In our tests, $S_I \sim I^\gamma$

where γ = 1.6 – 2.1 for all measured devices, confirming that 1/f noise is caused by fluctuations in the resistance (Figure S11a).

We also studied the gate-dependence of 1/f noise characteristics to understand the origins of the low frequency fluctuations and the relative role of contacts in MoS_2-graphene and MoS_2-metal devices. Figure 3b shows 1/f behavior of a MoS_2-graphene device for V_g = -40 to 70 V. Noise spectral density shows $1/f^{\beta}$ behavior (β = 0.97 – 1.2) with no clear dependence on V_g over the whole range (see inset of Figure 3c). Transfer characteristics (I_d – V_g) of this device show a threshold voltage V_{th} = 40 V (Figure 3c), and thus measurements cover both accumulation ($V > V_g - V_{th}$) and sub-threshold regions ($V < V_g - V_{th}$). The noise amplitude A was extracted from the plots of I^2/S_I versus frequency with the V_g dependence analyzed in Figure 3c,d. First, 1/A varies linearly with V_g in the accumulation region (Figure 3c), even though I_d follows a super-linear behavior with V_g in accumulation. Note that $I \sim V_g^{m}$ (m = 1 – 2) behavior arises from reduced screening effect in a two-dimensional material with parabolic band structure and has been described in experimental findings[24] and in analytical calculations.[25] Within Hooge's mobility fluctuation model, the noise amplitude A is related to the carrier number (N) according to A = α_H/N, where α_H is Hooge's parameter and N = $C_g/(V_g - V_{th})/q$ in the accumulation region, where C_g is total gate oxide capacitance and q is electronic charge. Thus, the linear 1/A ~ V_g dependence in the accumulation regime in Figure 3c and strong correlation between noise amplitude and current throughout the whole range of V_g suggests mobility fluctuation or correlated mobility-number fluctuation as the dominant source of current fluctuations in the accumulation region, in agreement with previous 1/f noise studies conducted on exfoliated MoS_2 transistors.[26] The number fluctuation model predicts the correlation between A and $(g_m/I)^2$, where g_m is the transconductance. [27–30] In the absence of such correlation in these devices, we rule out the number fluctuation model. The

Hooge parameter for this device was extracted as $\alpha_H = 0.21$, which is comparable to previous CVD-grown MoS_2[31] but larger than high quality exfoliated MoS_2 by up to 2 orders of magnitude.[26] Indeed, the average Hooge parameter of six measured devices is 0.33 ± 0.08.

Now we consider the role of contacts in the 1/f noise behavior in graphene-MoS_2 and metal-MoS_2 devices. In the case of significant Schottky barriers at the contacts, fluctuations in both channel resistance (R_{ch}) and contact resistance (R_c) can contribute to the overall noise in the transistor. Thus, the normalized noise spectral density can be written as:

$$\frac{S_I}{I^2} = \frac{S_{R_c}}{R_c{}^2}\frac{R_c^2}{(R_{ch} + R_c)^2} + \frac{S_{R_{ch}}}{R_{ch}{}^2}\frac{R_{ch}^2}{(R_{ch} + R_c)^2}$$

where S_{R_c} and $S_{R_{ch}}$ are power spectral density originating solely from the contacts and the channel, respectively. Based on this equation for the number fluctuation model, in the case of dominant channel resistance, noise A (and S_I/I^2) would vary as $\sim V_g{}^2$, and in the case of dominant contact resistance, the noise would result in $\sim V_g{}^{-2}$ dependence in the accumulation region. In our results, A versus V_g behavior follows $V_g{}^m$ ($m = 1 - 2$, see Figure S11b in the SI file). Note that a log-log plot of A versus ΔV_g overestimates the exponent m in Figure 3d. However, the A versus V_g behavior is starkly different from the $\sim V_g{}^2$ behavior expected for dominant contact resistance that has been seen in previous CVD-grown MoS_2 transistors.[32] Thus, we can conclude that the MoS_2-graphene interface is not the dominant source of 1/f noise in our devices.

Now we discuss control MoS_2-metal devices and directly compare the noise metrics between two kinds of devices. Noise spectral density follows I^γ/f^β behavior in all MoS_2-metal devices with exponent $\beta = 1 \pm 0.2$ and $\gamma = 2 \pm 0.3$ (Figure S12a,b). 1/A dependence on V_g is also linear in the accumulation region, suggesting the validity of the mobility fluctuation model

(Figure S12c). The average Hooge parameter for four measured MoS_2-metal devices was found to be 4.59 ± 2.58, an order of magnitude higher than MoS_2-graphene devices. Note that the Hooge parameter of the present MoS_2-metal devices is higher than values reported in the literature on CVD-grown MoS_2.[33] However, the present MoS_2-graphene and MoS_2-metal devices use MoS_2 grown under identical conditions and undergo the same processing steps. Thus, reduced noise could be correlated to superior contact (as shown by transport and KPFM experiments) in lateral MoS_2-graphene devices. Further evidence of larger current fluctuations is seen in Figure S12d, which shows a dip in $1/A$ versus V_g behavior for some MoS_2-metal devices. Such a peak has been seen before in bilayer MoS_2 and V, M, and Λ-shaped noise dependence on carrier density in single- and few-layer graphene.[34,35] Thus, the dip in $1/A$ can be explained within a model that takes into account the van der Waals gap between MoS_2 and traps inside SiO_2 that results in noise increasing with N at low N and decreasing with N at high N. Overall, the absence of such a dip in MoS_2-graphene devices suggests lower disorder possibly from the contacts.

Finally, we compare the normalized noise amplitude ($A \sim 1/N$) with the total number of carriers (i.e., channel area $L \times W$) for all measured MoS_2-graphene and MoS_2-metal devices (Figure 4). V_g dependence of normalized noise amplitude shows overall decreased noise in MoS_2-graphene. Furthermore, channel area-scaling results in a tighter distribution of noise metrics for MoS_2-graphene devices (Figure 4), suggesting MoS_2-metal has a larger contribution of noise from the contacts. Furthermore, the overall V_g dependence is more well-defined ($A \sim 1/V_g$) in MoS_2-graphene devices, again corroborating the dominance of channel resistance fluctuations compared to contact resistance fluctuations.

For reliable electronics, it is also critical to achieve mechanically and electrostatically robust contacts. The present MoS_2-graphene devices have essentially a 1D interface between two 2D

materials. Thus far, electrostatic breakdown of a lateral heterojunction of this type has not been probed. Figure 5a, b shows current-voltage characteristics of a MoS_2-graphene and a MoS_2-metal device for V_d = 75 to -75 V (sweep rate = 1 V/s) under vacuum (pressure < 10^{-5} torr). Both devices show qualitatively similar behavior of electrostatic breakdown. In particular, the current decreases irreversibly by more than 2 orders of magnitude within 1 V. Interestingly, both MoS_2-graphene and MoS_2-metal devices show comparable maximum width-normalized drain current (~40 μA/μm) just before breakdown, roughly an order of magnitude lower current density than high quality exfoliated monolayer MoS_2.[36] The breakdown field of the two devices is also comparable (~38 MV/m). Scanning electron microscopy of the broken devices was conducted to probe morphological evidence of the failure mode (inset of Figure 5a and b). A significant portion of CVD MoS_2 was found missing near the drain contacts in both of the devices. This suggests a similar failure mechanism irrespective of metal or lateral graphene contacts. Thus, direct growth of the MoS_2-graphene heterojunction does not significantly affect the electrostatic breakdown characteristics of the devices.

To shed light on the origin of the improved electrical performance of the MoS_2-graphene devices, we perform bandstructure, band alignment, and transport calculations. The total resistance (R_{tot}) of the device between source and drain is comprised of the series resistances from the graphene grains (R_{grap}, forming source and drain), resistance of MoS_2 grain (R_{MoS_2}, constituting the channel) and resistances of the interfaces ($R_{int.}$) between graphene and MoS_2. We calculate the series grain resistances of graphene and MoS_2 sections from the general expression– $R_{2D} = \rho \frac{L}{W}$, where ρ is the resistivity of the material (sheet resistance in this case) and $\frac{L}{W}$ is the aspect ratio of the sample. The conductivity ($\sigma = \frac{1}{\rho}$) of graphene and

MoS$_2$ grain is calculated from $\sigma = qn\mu$, where n is the sheet charge density, μ is the carrier mobility (mobility calculation is further elaborated in the Experimental Section).

The calculation of interface resistance involves four steps: bandstructure calculations for each graphene and MoS$_2$ from first principles, band alignment at the interface based on the Schottky-Mott rule, calculation of electron transmission across the interface from energy and momentum conservation at the interface, and finally computing the interface resistance in the Landauer formalism.

Density Functional Theory (DFT) supercell calculations are widely used in the literature for vertical heterostructures as well as lateral heterostructures[37,38] formed by more commensurate materials like hBN-graphene. However, performing extended supercell calculations for lateral interface formed by highly incommensurate materials such as graphene-MoS$_2$ becomes computationally very expensive[39]. In this work, we first calculate the electronic band structure of graphene and MoS$_2$ individually using first-principles DFT as implemented within the open-source distribution Quantum-Espresso[40] (further details on the DFT calculations are given in the Experimental Section). The calculated band structures and densities of states (DOS) are shown in Figure S13a and b, respectively. Then we align the bands at the interface using a semi-classical Schottky-Mott rule, where the vacuum levels are matched at the interface and bands are aligned using their respective electron affinities and work functions. Several papers show that band alignment in 2D lateral heterojunctions follows the Schottky-Mott rule and that the band alignment is relatively insensitive to the interfacial details when the overall dimensions of the device are much larger than the characteristic junctions width[41,39,42] as is the case in our samples. The difference in work function (ϕ) and the electron affinity (χ) of graphene and MoS$_2$ results in the formation of an energy barrier (ϕ_B) at the interface. As graphene is essentially metallic, the bands bend only

on the MoS$_2$ side near the interface to account for the energy barrier height. The resulting band structure alignment at the interface for zero gate voltage is shown in Figure S13. Further details on how the two band structures are aligned at the interface under extrinsic (gated) conditions are given in Figure S14.

On aligning the bands at the interface, we developed a numerical model to calculate the transmission coefficient of electrons over the energy barrier from graphene to MoS$_2$. In our model, we include both the effect of the potential barrier at the interface and the mismatch in the electronic band structures of the two materials by simultaneously conserving the energy as well as the component of the wavevector parallel to the interface. This approach, which is an extension of the method originally proposed by Yazyev and Louie[43] for electron transmission through graphene-graphene grain boundaries, allows us to calculate the dependence of interfacial resistance between graphene and MoS$_2$ on the band alignment between the two domains at the heterojunction. Momentum conservation requires that the parallel component of the incident wave vector ($\mathbf{k}_{i_\parallel}$) be equal to the parallel component of the transmitted wave vector ($\mathbf{k}_{t_\parallel}$), in their respective domains; simultaneously, energy is conserved by finding a perpendicular component of the transmitted wave vector ($\mathbf{k}_{t_\perp}$), within the first Brillouin zone of MoS$_2$, such that $E_1(\mathbf{k}_i) = E_2(\mathbf{k}_{t_\parallel} + \mathbf{k}_{t_\perp})$. The mode-dependent transmission coefficient is then calculated using the perpendicular components of the incident ($\mathbf{k}_{i_\perp}$) and transmitted ($\mathbf{k}_{t_\perp}$) wave vectors using a general expression for wave transmission between two domains[44] are given by $\tau_b(\mathbf{k}_i) = \frac{4k_{i_\perp}k_{t_\perp}}{\left|k_{i_\perp} + k_{t_\perp}\right|^2}$, where b represents the electron band. Finally, we obtain the energy-resolved values of the transport distribution function (TDF), $\Xi(E)$, from the transmission coefficient and velocity as $\sum_b v_b(E)\, \Gamma_b(E) D_b(E)$, where $D_b(E)$ represents density of states of bth band, by averaging

the product of transmission coefficient $\tau_b(\mathbf{k})$ and electron group velocity $v_b(\mathbf{k})$ over the constant energy contour, $\delta\left(E - E_b(\mathbf{k})\right)$, using the 2-dimensional version of the linear extrapolation approach described by Gilat and Raubenheimer[45] and then summing it over all electron bands (b):

$$\Xi(E) = \sum_b v_b(E)\,\Gamma_b(E)D_b(E) = \sum_b \frac{1}{4\pi^2}\int v_b(k)\,\tau_b(k)\,\delta\left(E - E_b(\mathbf{k})\right)d\mathbf{k}$$

The TDF is then used to numerically calculate the interfacial conductance using Landauer formalism and inverted to obtain the interfacial resistance $R_{int.}$ as

$$R_{int.}^{-1} = G_{int.} = \frac{e^2}{2}\int_{E_C}^{E_{max}} \Xi(E)\left(-\frac{\partial f(E - E_F, T)}{dE}\right)dE,$$

where E_C is the bottom of the conduction band, E_{max} is the highest electron energy among the bottom four conduction bands and f is the Fermi-Dirac distribution function, $f(E) = [1 + \exp(E - E_F/k_BT)]^{-1}$.

In the case of a finite gate voltage and zero drain bias, the Fermi levels in both graphene and MoS$_2$ away from the interface shift relative to their position at zero gate voltage in response to the induced charge in the 2-dimensional layers, as shown in Figure 6a. Consequently, the energy bands on both sides of the interface rearrange themselves to maintain the equilibrium condition. However, the shift in the bands on the two sides is not identical because the two materials have different densities of states (DOS, Figure S13 b), leading to an increase in band bending in the MoS$_2$ with increasing gate bias. The transmission coefficient of electrons across the interface, however, depends on the alignment of energy bands of graphene and MoS$_2$ at the interface. For example, states near the Fermi level in graphene cannot typically be transmitted because there are no available states at the same energy in MoS$_2$ as energies near the Fermi level fall inside the bandgap. Increasing the gate bias increases the sheet

charge density in both graphene and MoS_2; in response, the barrier height at the junction of the two domains decreases with increasing gate voltages (Figure 6a), in agreement with the electrical measurements in Figure 1i.

As a result of band rearrangement and barrier lowering, the transmission $\Gamma(E)$ also shows a dependence on gate voltages. It can be seen in Figure 6b that with increasing gate voltages, the transmission coefficient $\Gamma(E)$ shifts towards the left resulting in larger overlap between $\Gamma(E)$ and the so-called Fermi window $\left(-\frac{df}{dE}\right)$, centered at the Fermi level. An increase in overlap between the transmission $\Gamma(E)$ and the Fermi window corresponds to a reduction in interfacial resistance. In addition to the reduction in interfacial resistance with gate voltage, we obtain a reduction in the resistance of the MoS_2 due to the increase in sheet charge density and mobility with gate voltage (conductance calculation described further in Experimental Section). The simultaneous reduction in interfacial resistance and MoS_2 resistance with gate bias leads to an overall decrease in the total resistance (R_{tot}), as can be seen in Figure 6c. We find that the contribution of the interfacial resistance to the total resistance of the combined MoS_2+interface+graphene system (R_{tot}) decreases with increasing gate voltages, starting at around 25% of the total in the intrinsic case (zero gate bias), and rapidly dropping below 1% at gate voltage of 60 V, as shown in the inset of Figure 6c, further corroborating the KPFM measurements at the interface. The agreement between measured and calculated total resistances of the device, mathematically written as $R_{tot} = 2R_{grap} + R_{MoS_2} + 2R_{int.}$ and shown in Figure 6d, indicates that the measured resistances are well reproduced by the model. We also show that at large non-zero gate biases, the interface contributes very little to the overall resistance, leading to Ohmic behavior.

3. CONCLUSION

15

In conclusion, we report seed-free synthesis of graphene and MoS_2 lateral heterojunctions through the CVD method, which exhibit improved electrical performance compared to conventional metal-contact MoS_2 devices. This method makes in-plane MoS_2-graphene heterostructures promising for the large-scale production of electronic and logic circuits from all-2D materials for next generation device applications. Temperature-dependent electrical characterization shows Ohmic behavior for the MoS_2-graphene FET devices at back-gate voltages above 60 V, verifying a high-quality lateral interface between MoS_2 and graphene. KPFM results also visualize the reduction of the MoS_2-graphene in-plane junction resistance at positive gate voltages. We further present the first study of 1/f noise in 2D lateral heterojunction electronic circuits. MoS_2-graphene devices show up to an order of magnitude lower noise amplitude in comparison to MoS_2-metal devices fabricated under similar conditions. A systematic study of 1/f noise by varying gate bias and area-scaling revealed the dominant origin of noise as mobility fluctuations in the accumulation region. We also conducted the first electrostatic breakdown study of lateral MoS_2-graphene heterojunctions. In this case, MoS_2-graphene and MoS_2-metal devices showed comparable current density, breakdown fields, and similar failure modes through microscopic visualization. Our numerical calculations reveal that both the barrier at the interface as well as the resulting interfacial resistance decrease as sheet charge is increased in response to the external gate voltage, matching the KPFM results. At gate voltages above 60 V, the interface contributes less than 1% to the overall device resistance despite the appreciable electron mobility in MoS_2, resulting in the observed linear (Ohmic) behavior.

4. EXPERIMENTAL SECTION

Graphene growth procedure: The Three-Zone MTI CVD furnace[46] is used for graphene growth. The partially and fully covered graphene films are grown on the copper substrate (Alfa Aesar, product no. 46365) by using atmospheric pressure CVD growth process. The copper substrate is immersed inside of the hydrochloric acid for 15 minutes to remove the

local surface oxides and then rinsed with acetone and isopropanol. Next, the copper substrate was placed inside of the CVD furnace and then the chamber was evacuated to the 1 mTorr vacuum pressure to remove the unwanted gasses. The chamber was then restored to atmospheric pressure by filling it with 5% hydrogen diluted in argon gas. The growth procedure consists of three main steps. The first step was annealing, in which the maximum temperature of the furnace is set to 1050 ^{o}C and the annealing time was 1 hour for the growth of both partially and fully covered graphene films. In the second step, The furnace was filled with 20 p.p.m methane gas and the growth time was 60 minutes for partial coverage graphene and 90 minutes for full coverage graphene film. The third step was cooling in which the furnace is cooled down to room temperature by force cooling and the methane gas also was stopped from flowing into the furnace.

Growth process of CVD MoS₂ on graphene/SiO₂/Silicon substrate: The oxygen plasma treatment is performed on SiO₂/Silicon substrate for two minutes to make the substrate hydrophilic, which helps with the transfer of the graphene film and the growth of MoS₂ on the substrate. After transferring the partial coverage graphene film onto the SiO₂/Silicon substrate, the substrate is annealed at 400 ^{o}C for 8 hours. The 5% diluted hydrogen in argon gas was also continuously supplied during the annealing process to remove the residue of the transfer process. Then, the substrate is placed inside of the MoS₂ CVD chamber together with 2 milligrams of Molybdenum trioxides and 1 gram of sulfur as precursors for the MoS₂ growth. The chamber temperature increased to 550 ^{o}C in 30 minutes and then it was increased to 850 ^{o}C in 60 minutes. The growth time was 10 minutes and then furnace was cooled down to the room temperature by natural cooling. It is worth mentioning that increasing the time of the MoS₂ growth or the amount of the MoO₃ powder will result in the growth of the MoS₂ film on top of the graphene film.[47]

Fabrication of the MoS₂-graphene field effect transistors (FETs): After the graphene film was transferred onto the SiO₂ substrate, it was patterned into rectangles by a photolithography process followed by oxygen plasma etching. Next, MoS₂-graphene heterostructure was synthesized, and the metal electrodes were patterned on the MoS₂-graphene FETs and on the MoS₂ FETs by an electron beam lithography method. Finally, 10 nm Titanium and 60 nm Gold were deposited on the devices by an electron beam evaporation process.

KPFM: All AFM experiments were carried out with a Dimension ICON system (Bruker, CA) in ambient conditions. PFQNE-AL cantilevers (Bruker, CA) were selected for improved spatial resolution in surface potential measurements. The nominal spring constant is 0.8 N/m and the resonant frequency is 300 kHz. Two-pass technique (also known as 'lift mode') was applied in KPFM experiments. During scanning, the sample was grounded, while a bias $\Delta V = V_{DC} + V_{AC}$ was applied to the AFM cantilever, where the V_{DC} and V_{AC} are the DC and AC component, respectively. The frequency of V_{AC} was chosen at the resonant frequency of the cantilever. The AFM controller nulled the cantilever amplitude due to periodic electrostatic force by adjusting V_{DC}. If the work function of the cantilever tip Φ_{tip} is known, then the sample work function Φ_s can be given as $\Phi_s = \Phi_{tip} - eV_{DC}$. Φ_s and V_{DC} are

opposite in sign, so the work function Φ_s has inverse contrast with KPFM mapping. All AFM data were analyzed with Nanoscope Analysis software (Bruker, CA).

1/f noise and breakdown measurements: All 1/f noise and breakdown measurements were carried out under vacuum (pressure ~10^5 torr) using a LakeShore CRX 4K probe station. The current fluctuations were amplified with a low-noise voltage amplifier (DL Instruments 1212) and power spectral density was captured with a spectrum analyzer (Stanford Research SR780). Drain and gate voltage were controlled by Keithley Instruments 2400 source-meters and homemade LabView programs. Power spectral density in devices powered by stand-alone batteries and source-meters was found to be comparable, thus confirming that the measurement apparatus does not contribute to the measured noise.

Raman mapping: The Swift mode Raman mapping with a 500 nm scanning step size is performed for two different ranges with the total number of 1824 collected spectrums. The first range was from 100 cm^{-1} to 900 cm^{-1} and the second one was from 800 cm^{-1} to 1700 cm^{-1}.The classical least-square (CLS) fitting was used to analyze the Raman data, which includes the E^2_g and A^1_g peaks of the MoS$_2$ and the G peak of the graphene.

Density functional theory calculation of the electronic structures: We performed self-consistent Density Functional Theory (DFT) calculations with the open-source software Quantum-Espresso (www.quantum-espresso.org). For graphene, we used a scalar relativistic, norm-conserving pseudopotential (NCPP) which uses a direct-fit Von Barth-Car method with a Perdew-Zunger (LDA) exchange-correlation functional. For MoS$_2$, we used a non-relativistic NCPP for Mo and a scalar relativistic NCPP for S. Both potentials employed a Martins-Troullier method with a Perdew-Wang (LDA) exchange-correlation. The lattice constants are a=2.459 Å for graphene and a=3.125 Å, z=3.11 Å for MoS$_2$, where z is the S-S distance. The band structures produced by these parameters can be found in Figure S13. To capture the monolayer band structure, planes of single-layer graphene or tri-layered MoS$_2$ are separated by a 20 Å vacuum. The cutoff energy for plane waves was 120 Ry for graphene and 140 Ry for MoS$_2$. We used a convergence threshold of 10^{-16} on a Monkhorst-Pack grid sizes of 8 × 8 × 1 for graphene and 6 × 6 × 4 for MoS$_2$ for the initial total energy calculation and then performed a bands calculation on a dense grid of 126,040 k-points with a convergence threshold of 10^{-12}. We use the central difference method to obtain the band velocities per band which in turn is used to determine the electronic DOS and other transport properties including interfacial transmission and resistance of the interface.

Mobility calculation in MoS$_2$: The carrier mobility in graphene, which depends on its carrier concentration, is taken from the work by Dorgan et al.[48] In addition to intrinsic phonon-limited carrier mobility in MoS$_2$ (μ_{ph}~ 410 cm^2/V-s[49]), the mobility is also influenced by factors like charged impurities, surface optical (SO) phonons and other short range scattering mechanisms. However, it has been reported that the electron mobility in MoS$_2$ is largely affected by the charged-impurity (CI) scattering.[50–52] An empirical expression for CI-limited mobility for MoS$_2$ has been adopted and modified from the work by Ma and Jena[52] and is

18

given as: $\mu_{CI} \approx \frac{45}{n_{imp}/10^{11}\ cm^{-2}} \left(A(\epsilon) + \left(\frac{C_{oxide}V_g + n_{imp}}{10^{13}\ cm^{-2}} \right)^{1.2} \right)$, where A($\epsilon$)=0.036 is a fitting constant depending on the dielectric constant of SiO$_2$ (oxide layer), C_{oxide} is the capacitance per unit area of the gate oxide, and n_{imp} is the charged-impurity density. The impurity density equals sheet charge density ($n_C = C_{oxide}V_g + n_{imp}$) at zero gate voltage. We use an impurity concentration of $5.5 \times 10^{11}\ cm^{-2}$, which is found by fitting the finite resistance at zero gate voltage obtained from experimentally measured $I_d - V_{DS}$ data. In the presence of multiple scattering mechanisms, the mobility of the free carriers can be represented by Matthiessen's rule and is given as: $\mu_{MoS_2} = \left(\mu_{ph}^{-1} + \mu_{CI}^{-1} + \mu_{SR}^{-1} \right)^{-1}$, where μ_{SR} is the mobility due to short range effects.[51]
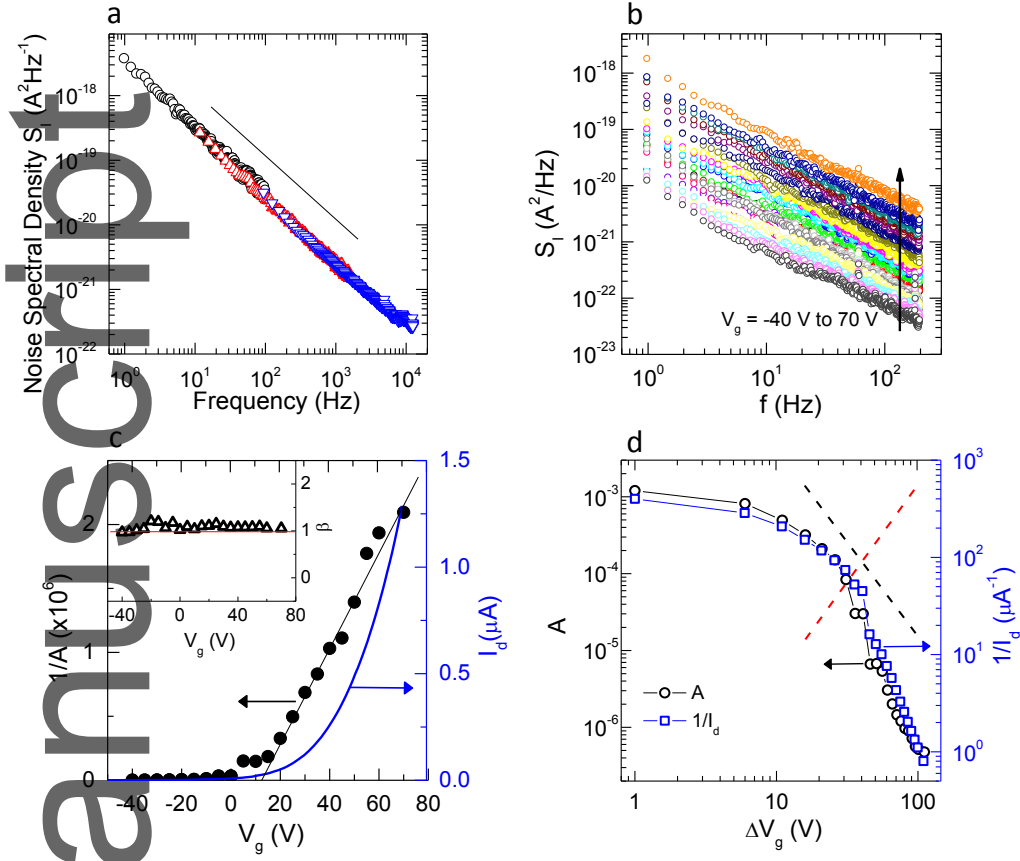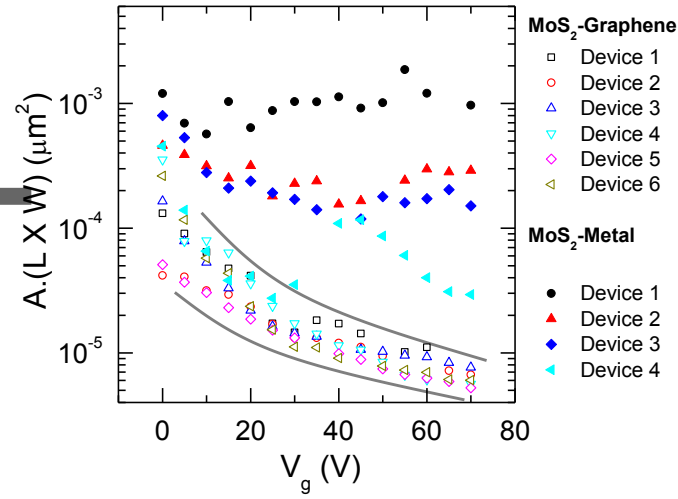
FIGURES
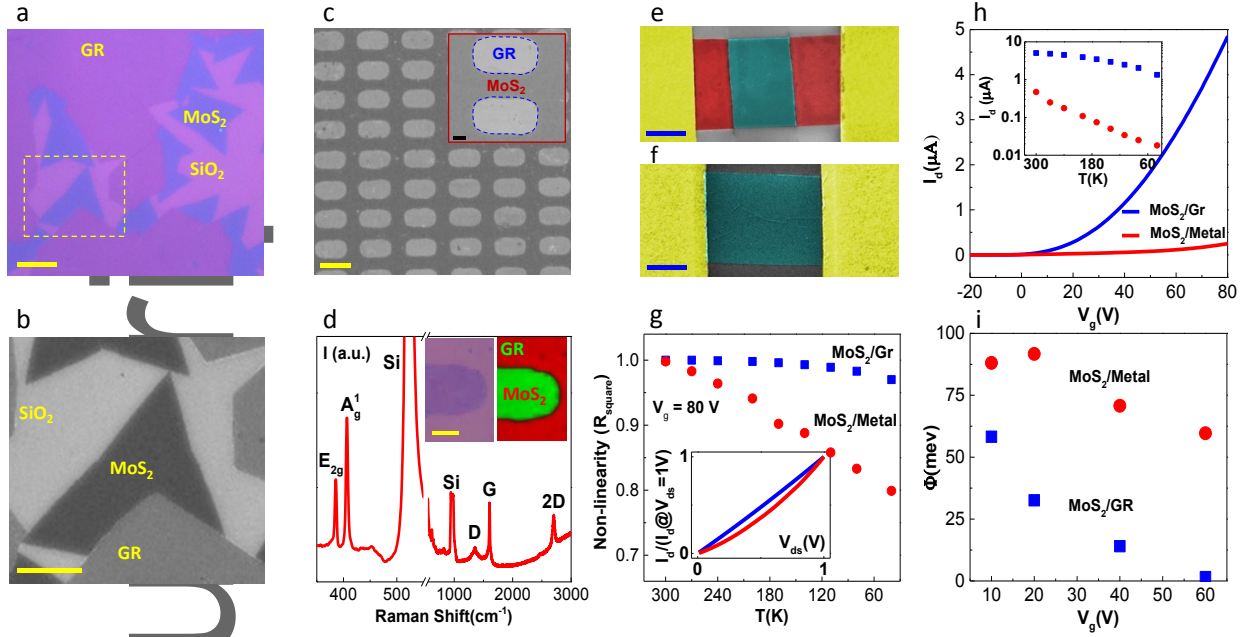
Figure 1: Characterization of the MoS$_2$-graphene in-plane heterostructure. **(a)** Optical image of the partially covered MoS$_2$ triangular flakes next to the graphene flakes (scale bar 10 µm). **(b)** SEM image of the MoS$_2$-graphene in-plane heterostructure from the selected area in (a) (scale bar 5 µm). **(c)** SEM image of a large scale patterned MoS$_2$-graphene in-plane heterostructure (scale bar 10 µm) the inset magnifies the same image (Scale bar in inset 2 µm). **(d)** A representative Raman point spectra from the MoS$_2$-graphene interface area. The inset shows optical image and Raman mapping of a patterned MoS$_2$-graphene heterostructure. The scale bar is 2 µm. **(e-f)** SEM images of the MoS$_2$-graphene and MoS$_2$-metal FETs, respectively (scale bars 2 µm and 1 µm, respectively). **(g)** The linear regression (R$_{square}$) of the I$_d$-V$_{sd}$ at different temperatures for the MoS$_2$-graphene and MoS$_2$-metal FETs (The inset shows normalized I$_d$-V$_{sd}$ characteristics of the both devices – normalized with their respective I$_d$ at V$_{sd}$=1V). **(h)** I$_d$-V$_g$ characteristics of the MoS$_2$-graphene and MoS$_2$-metal FETs at 270 K (the inset shows the drain current at V$_g$=80V with respect to temperature). **(i)** Extracted Schottky barrier height - extracted from Arrhenius measurements - as a function of V$_g$ for the MoS$_2$-graphene and MoS$_2$-metal FETs.
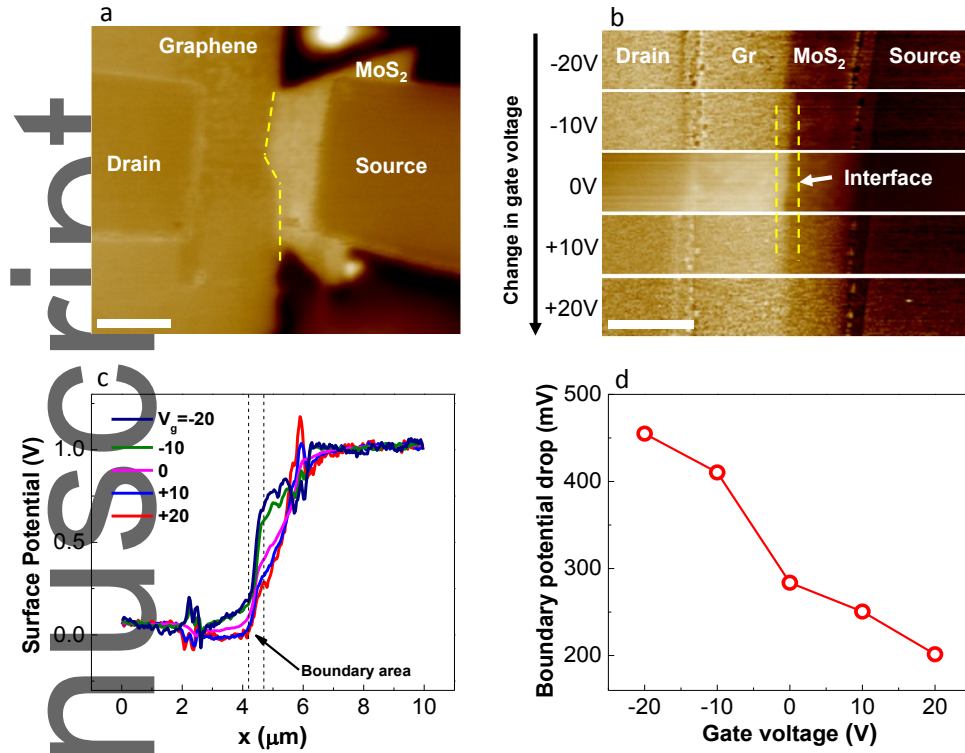
Figure 2: KPFM measurements. **(a)** KPFM mapping of the MoS$_2$-graphene transistor with $V_{gate} = 0\,V$ and $V_{sd} = 0\,V$. The interface between graphene and MoS$_2$ is highlighted with yellow dashed line (scale bar 2 µm). **(b)** KPFM mapping of the interface area from a selected region shown in (a) by keeping $V_{sd} = 1\,V$ and changing V_{gate} from $-20\,V$ to $+20\,V$ with $10\,V$ increments (Scale bar 2 µm). The dashed lines show the interface area. **(c)** Corresponding surface potential profiles across the interface area. **(d)** The potential drop at the interface area as a function of the applied gate voltages.

Figure 3. 1/f noise measurements of MoS$_2$-graphene and MoS$_2$-metal FETs. **(a)** Noise spectral density (S_I) as a function of frequency for a MoS$_2$-graphene FET at V_g = 60 V and V_d = 4 V showing 1/f^β behavior with β = 1.02 ± 0.002. The black line shows ideal 1/f behavior. **(b)** S_I versus frequency of the device at V_g varying from -40 V to 70 V at V_d = 2 V. **(c)** Inverse of noise amplitude (1/A) versus V_g compared with transfer characteristics (device current (I_d) versus V_g) from the data in (c). The inset shows β as a function of V_g. **(d)** Log-Log plot of A and 1/I_d versus ΔV_g (= V_g + 41) where V_g is ranging from -40 to 70 V. Black and red dashed lines show V_g^{-2} and V_g^2 dependence for purely channel and purely contact effects on 1/f noise, respectively.

Figure 4: Comparison of area-normalized noise amplitude (A.(L X W)) of MoS$_2$-graphene and MoS$_2$-metal FETs as a function of V_g. Two gray lines show upper and lower bonds of noise amplitude for MoS$_2$-graphene devices.

23
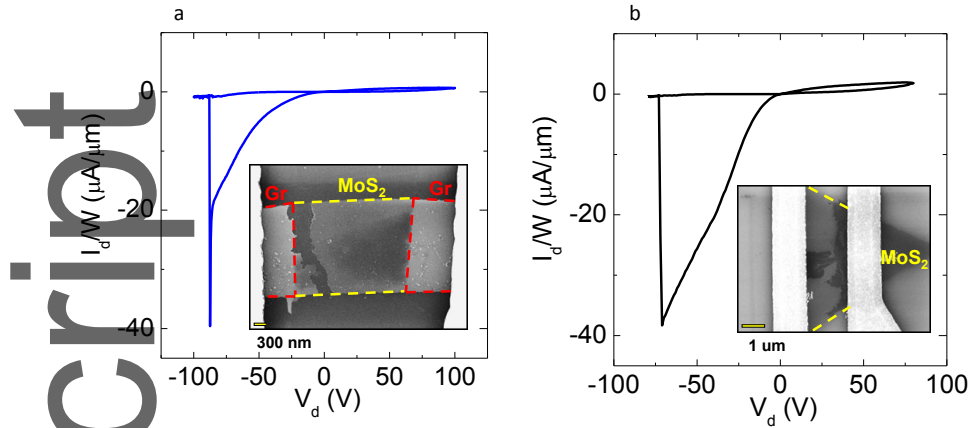
Figure 5: Breakdown study of MoS₂-graphene and MoS₂-metal FETs. (a), (b) Current-voltage characteristics of a MoS₂-graphene and MoS₂-metal FET, respectively, at $V_g = 0$ V showing irreversible breakdown at large V_d. The current was normalized to the channel width. The insets of figure (a) and (b) show scanning electron microscopy micrographs of the MoS₂-graphene and MoS₂-metal FETs after the breakdown, respectively.
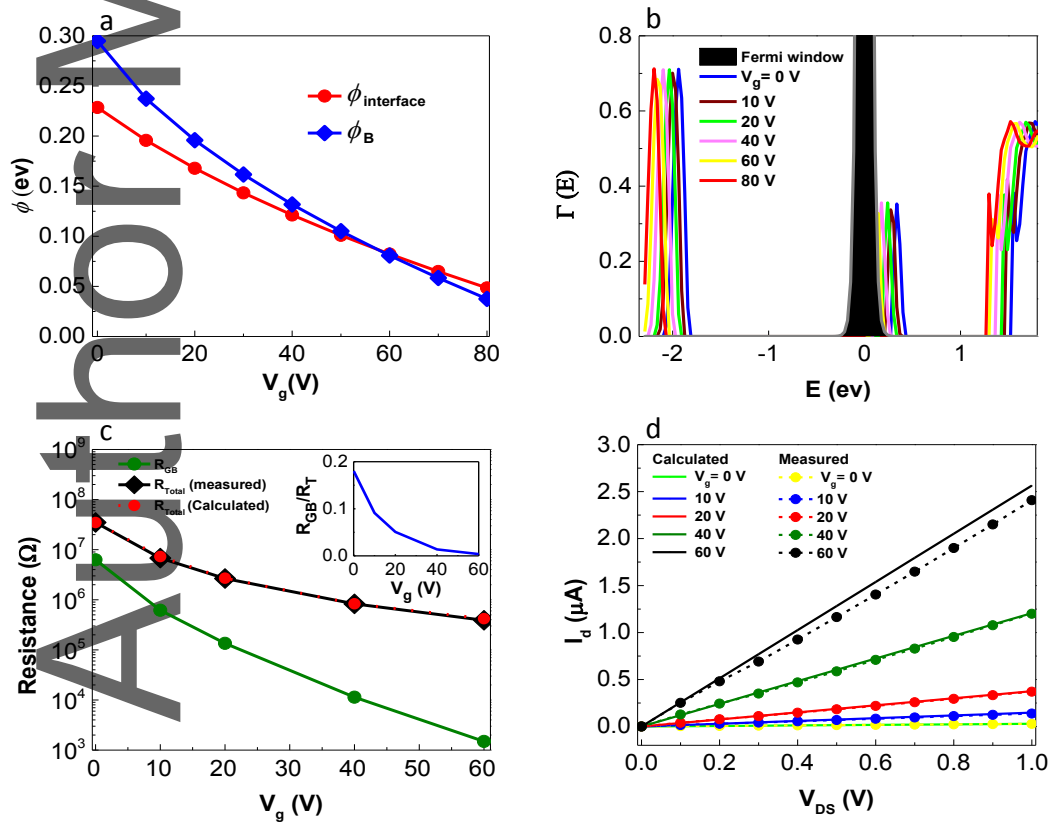
Figure 6: DFT calculations. **(a)** Variation in interfacial Schottky potential barrier height —— from graphene to MoS_2 (ϕ_B) and from MoS_2 to graphene ($\phi_{interface}$) — with gate voltage (V_g). **(b)** Resulting shift in transmission coefficient with gate voltage, such that with the increasing V_g a larger part of $\Gamma(E)$ overlaps with the Fermi window (shown by the grey area in the plot) resulting in increased conductance. **(c)** Interfacial resistance ($R_{int.}$) and the total resistance (R_{tot}) —— both measured (red line with red markers) and calculated (black line with black markers) —— against gate voltage. The inset shows the percentage contribution of interfacial resistance ($R_{int.}$) towards the total resistance (R_{tot}) of the device at different gate voltages, in good agreement with KPFM measurements. **(d)** Drain current (I_D) vs. drain-source voltage (V_{DS}) calculated both experimentally and by numerical simulation showing good agreement between numerical and experimental results.

Supporting Information: Supporting Information is available from the Wiley Online Library.

Authors Contributions: A.S.K. and A.B. conceived the idea. A.S.K led the material synthesis, device fabrications, electrical measurements and device characterizations. A.B. synthesized the MoS_2-graphene lateral heterostructure and performed electrical experiments. A.B. and P.Y. carried out device fabrications and characterizations. P.Y. and T.F. synthesized the CVD graphene. A.K.M. performed band structure alignment, mobility, and interfacial resistance calculations. V.K.S performed 1/f noise and breakdown measurements and analysis. C.J.F. carried out DFT and transmission coefficient calculations. Z.A. conceived and supervised the calculations. M.C.H supervised the 1/f noise and breakdown measurements and analysis. F.L. performed KPFM measurements and R.S.Y supervised him. S.F. helped in DFT calculations. M.H. helped in CVD MoS_2 and graphene synthesis. The lead authors acknowledge the assistance of Dr. Daniel P. Bailey in copy-editing this manuscript.

REFERENCES

[1]   G. E. Moore, *Solid-State Circuits Soc. Newsletter, IEEE* **2006**, *20*, 36.

[2]   S. Najmaei, Z. Liu, W. Zhou, X. Zou, G. Shi, S. Lei, B. I. Yakobson, J.-C. Idrobo, P. M. Ajayan, J. Lou, *Nat. Mater.* **2013**, *12*, 754.

[3]   Y. Zhan, Z. Liu, S. Najmaei, P. M. Ajayan, J. Lou, *Small* **2012**, *8*, 966.

[4]   P. Yasaei, B. Kumar, T. Foroozan, C. Wang, M. Asadi, D. Tuschel, J. E. Indacochea, R. F. Klie, A. Salehi-Khojin, *Adv. Mater.* **2015**, *27*, 1887.

[5]   Y. Zhang, Y. Zhang, Q. Ji, J. Ju, H. Yuan, J. Shi, T. Gao, D. Ma, M. Liu, Y. Chen, X. Song, H. Y. Hwang, Y. Cui, Z. Liu, *ACS Nano* **2013**, *7*, 8963.

[6]   X. Li, W. Cai, J. An, S. Kim, J. Nah, D. Yang, R. Piner, A. Velamakanni, I. Jung, E. Tutuc, S. K. Banerjee, L. Colombo, R. S. Ruoff, *Science (80-.).* **2009**, *324*, 1312.

[7]   F. Xia, H. Wang, Y. Jia, *Nat. Commun.* **2014**, *5*, 4458.

[8]   Q. H. Wang, K. Kalantar-Zadeh, A. Kis, J. N. Coleman, M. S. Strano, *Nat. Nanotechnol.* **2012**, *7*, 699.

[9]   R. Ganatra, Q. Zhang, *ACS Nano* **2014**, *8*, 4074.

[10]   B. Radisavljevic, a Radenovic, J. Brivio, V. Giacometti, a Kis, *Nat. Nanotechnol.* **2011**, *6*, 147.

[11]   S. Das, H. Y. Chen, A. V. Penumatcha, J. Appenzeller, *Nano Lett.* **2013**, *13*, 100.

[12]   R. Kappera, D. Voiry, S. E. Yalcin, B. Branch, G. Gupta, A. D. Mohite, M. Chhowalla, *Nat. Mater.* **2014**, *13*, 1128.

[13]   L. Yu, Y. H. Lee, X. Ling, E. J. G. Santos, Y. C. Shin, Y. Lin, M. Dubey, E. Kaxiras, J. Kong, H. Wang, T. Palacios, *Nano Lett.* **2014**, *14*, 3055.

[14]   Y. Liu, H. Wu, H.-C. Cheng, S. Yang, E. Zhu, Q. He, M. Ding, D. Li, J. Guo, N. O. Weiss, Y. Huang, X. Duan, *Nano Lett.* **2015**, *15*, 3030.

[15]   J. Yoon, W. Park, G. Y. Bae, Y. Kim, H. S. Jang, Y. Hyun, S. K. Lim, Y. H. Kahng, W. K. Hong, B. H. Lee, H. C. Ko, *Small* **2013**, *9*, 3295.

[16]   X. Cui, G.-H. Lee, Y. D. Kim, G. Arefe, P. Y. Huang, C. Lee, D. A. Chenet, X. Zhang, L. Wang, F. Ye, F. Pizzocchero, B. S. Jessen, K. Watanabe, T. Taniguchi, D. A. Muller, T. Low, P. Kim, J. Hone, *Nat. Nanotechnol.* **2015**, *10*, 534.

[17]   W. J. Yu, Z. Li, H. Zhou, Y. Chen, Y. Wang, Y. Huang, X. Duan, *Nat. Mater.* **2012**, *12*, 246.

[18]   P. Yasaei, B. Kumar, R. Hantehzadeh, M. Kayyalha, A. Baskin, N. Repnin, C. Wang, R. F. Klie, Y. P. Chen, P. Král, A. Salehi-Khojin, *Nat. Commun.* **2014**, *5*, 4911.

[19]   P. Yasaei, A. Fathizadeh, R. Hantehzadeh, A. K. Majee, A. El-Ghandour, D. Estrada, C. Foster, Z. Aksamija, F. Khalili-Araghi, A. Salehi-Khojin, *Nano Lett.* **2015**, *15*, 4532.

[20]   X. Ling, Y. Lin, Q. Ma, Z. Wang, Y. Song, L. Yu, S. Huang, W. Fang, X. Zhang, A. L. Hsu, Y. Bie, Y.-H. Lee, Y. Zhu, L. Wu, J. Li, P. Jarillo-Herrero, M. S. Dresselhaus, T. Palacios, J. Kong, **2015**, 30.

[21]   S. Jin-Hong Park, S. Lee, J. Jeon, S. Kyu Jang, S. Min Jeon, G. Yoo, Y. Hee Jang, J.-H. Park, *Nanoscale* **2015**, *7*, 1688.

[22]   H. Liu, M. Si, S. Najmaei, A. T. Neal, Y. Du, P. M. Ajayan, J. Lou, P. D. Ye, *Nano Lett.* **2013**, *13*, 2640.

[23]   J. R. Chen, P. M. Odenthal, A. G. Swartz, G. C. Floyd, H. Wen, K. Y. Luo, R. K. Kawakami, *Nano Lett.* **2013**, *13*, 3106.

[24]   S. Ghatak, A. N. Pal, A. Ghosh, *ACS Nano* **2011**, *5*, 7707.

[25]   S. Adam, S. Das Sarma, *Phys. Rev. B - Condens. Matter Mater. Phys.* **2008**, *77*, 1.

[26]   V. K. Sangwan, H. N. Arnold, D. Jariwala, T. J. Marks, L. J. Lauhon, M. C. Hersam, *Nano Lett.* **2013**, *13*, 4351.

[27]   S. Ghatak, S. Mukherjee, M. Jain, D. D. Sarma, A. Ghosh, *APL Mater.* **2014**, *2*, DOI 10.1063/1.4895955.

[28]   X. Xie, D. Sarkar, W. Liu, J. Kang, O. Marinov, M. J. Deen, K. Banerjee, *ACS Nano* **2014**, *8*, 5633.

[29]   J. Renteria, R. Samnakay, S. L. Rumyantsev, C. Jiang, P. Goli, M. S. Shur, A. A. Balandin, *Appl. Phys. Lett.* **2014**, *104*, 153104.

[30]   D. Sharma, M. Amani, A. Motayed, P. B. Shah, a G. Birdwell, S. Najmaei, P. M. Ajayan, J. Lou, M. Dubey, Q. Li, A. V Davydov, *Nanotechnology* **2014**, *25*, 155702.

[31]   H. J. Kwon, H. Kang, J. Jang, S. Kim, C. P. Grigoropoulos, *Appl. Phys. Lett.* **2014**, *104*, DOI 10.1063/1.4866785.

[32]   J. Renteria, R. Samnakay, S. L. Rumyantsev, C. Jiang, P. Goli, M. S. Shur, A. A. Balandin, *Appl. Phys. Lett.* **2014**, *104*, DOI 10.1063/1.4871374.

[33]   D. Sharma, M. Amani, A. Motayed, P. B. Shah, a G. Birdwell, S. Najmaei, P. M. Ajayan, J. Lou, M. Dubey, Q. Li, A. V Davydov, *Nanotechnology* **2014**, *25*, 155702.

[34]   H. N. Arnold, V. K. Sangwan, S. W. Schmucker, C. D. Cress, K. A. Luck, A. L. Friedman, J. T. Robinson, T. J. Marks, M. C. Hersam, *Appl. Phys. Lett.* **2016**, *108*, DOI 10.1063/1.4942468.

[35]   A. N. Pal, S. Ghatak, V. Kochat, A. Sampathkumar, S. Raghavan, A. Ghosh, *ACS Nano* **2011**, 2075.

[36]   D. Lembke, A. Kis, *ACS Nano* **2012**, *6*, 10070.

[37]   A. A. Kistanov, Y. Cai, Y.-W. Zhang, S. V Dmitriev, K. Zhou, *J. Phys. Condens. Matter* **2017**, *29*, 95302.

[38]   X. Liu, Z. Li, *J. Phys. Chem. Lett.* **2015**, *6*, 3269.

[39]   J. Zhang, W. Xie, J. Zhao, S. Zhang, *2D Mater.* **2016**, *4*, 15038.

[40]   P. Giannozzi, S. Baroni, N. Bonini, M. Calandra, R. Car, C. Cavazzoni, D. Ceresoli, G. L. Chiarotti, M. Cococcioni, I. Dabo, A. Dal Corso, S. de Gironcoli, S. Fabris, G. Fratesi, R. Gebauer, U. Gerstmann, C. Gougoussis, A. Kokalj, M. Lazzeri, L. Martin-Samos, N. Marzari, F. Mauri, R. Mazzarello, S. Paolini, A. Pasquarello, L. Paulatto, C. Sbraccia, S. Scandolo, G. Sclauzero, A. P. Seitsonen, A. Smogunov, P. Umari, R. M. Wentzcovitch, *J. Phys. Condens. Matter* **2009**, *21*, 395502.

[41]   H. Yu, A. Kutana, B. I. Yakobson, *Nano Lett.* **2016**, *16*, 5032.

[42]   Z. Lin, A. McCreary, N. Briggs, W. Zhang, Q. Wang, Y. Chen, A. Kumar, P. K. Ahluwalia, S. Zhu, Y. Ni, J. Liu, B. Ha Nguyen, V. Hieu Nguyen, B. Ram, A. Manjanath, A. K. Singh, J. Sophia Ponraj, Z.-Q. Xu, S. Chander Dhanabalan, Z.-K.

Tang, C.-J. Tong, W. Geng, X. Qian, Y. Wang, W. Li, C. Zhang, C. Gong, Y. Nie, K.-A. Min, C. Liang, Y. Jun Oh, H. Zhang, W. Wang, S. Hong, L. Colombo, R. M. Wallace, K. Cho, *2D Mater* **2017**, *4*, DOI 10.1088/2053-1583/4/1/015026.

[43]   O. V. Yazyev, S. G. Louie, *Nat. Mater.* **2010**, *9*, 806.

[44]   G. Chen, *Nanoscale Energy Transport and Conversion*, **2005**.

[45]   G. Gilat, L. J. Raubenheimer, *Phys. Rev.* **1966**, *144*, 390.

[46]   P. Abbasi, M. Asadi, C. Liu, S. Sharifi-Asl, B. Sayahpour, A. Behranginia, P. Zapol, R. Shahbazian-Yassar, L. A. Curtiss, A. Salehi-Khojin, *ACS Nano* **2017**, *11*, 453.

[47]   A. Behranginia, M. Asadi, C. Liu, P. Yasaei, B. Kumar, P. Phillips, T. Foroozan, J. C. Waranius, K. Kim, J. Abiade, R. F. Klie, L. A. Curtiss, A. Salehi-Khojin, *Chem. Mater.* **2016**, DOI 10.1021/acs.chemmater.5b03997.

[48]   V. E. Dorgan, M.-H. Bae, E. Pop, *Appl. Phys. Lett.* **2010**, *97*, 82112.

[49]   K. Kaasbjerg, K. S. Thygesen, K. W. Jacobsen, *Phys. Rev. B* **2012**, *85*, 115317.

[50]   Z. Yu, Z.-Y. Ong, Y. Pan, Y. Cui, R. Xin, Y. Shi, B. Wang, Y. Wu, T. Chen, Y.-W. Zhang, G. Zhang, X. Wang, *Adv. Mater.* **2015**, *4*, n/a.

[51]   Z. Yu, Y. Pan, Y. Shen, Z. Wang, Z.-Y. Ong, T. Xu, R. Xin, L. Pan, B. Wang, L. Sun, J. Wang, G. Zhang, Y. W. Zhang, Y. Shi, X. Wang, *Nat. Commun.* **2014**, *5*, 5290.

[52]   N. Ma, D. Jena, *Phys. Rev. X* **2014**, *4*, 11043.

Table of Content (TOC) Figure:
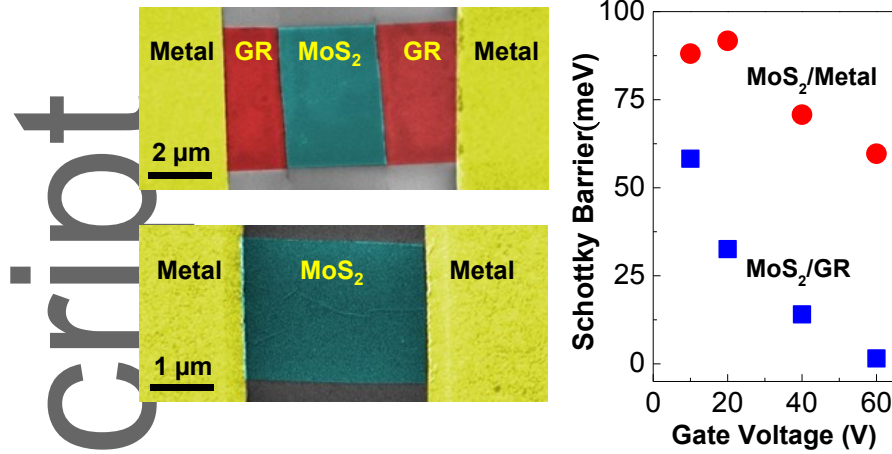
Table of Content (TOC) Text:

This paper reports extensive electrical characterization of lateral MoS$_2$-Graphene heterojunctions synthesized through seed-free consecutive chemical vapor deposition (CVD) processes. Device-level experiments, Kelvin probe force microscopy (KPFM) characterizations, and theoretical modeling show that the MoS$_2$-graphene field-effect transistors (FETs) exhibit an order of magnitude higher mobility and lower noise metrics compared with MoS$_2$-metal devices as a result of energy band rearrangement and smaller Schottky barrier height at the contacts. Overall, this work establishes the superlative electronic properties of directly grown MoS$_2$-graphene lateral heterostructures.